Journal of Magnetism and Magnetic Materials 558 (2022) 169522

Contents lists available at ScienceDirect

Journal of Magnetism and Magnetic Materials

journal homepage: www.elsevier.com/locate/jmmm

A study on the relationship of magnetic moments orientation in $L1_0$ FePt network nanostructured film by electron energy-loss magnetic chiral dichroism using semi-core excitation spectra

Hitoshi Makino [a], Ján Rusz [b], Jian Wang [c], Diego Turenne [b], Masahiro Ohtsuka [a,d], Yukiko K. Takahashi [c], Hermann A. Dürr [b], Shunsuke Muto [a,d,*]

[a] Department of Materials Physics, Graduate School of Engineering, Nagoya University, Furo-cho, Chikusa-ku, Nagoya 464-8603, Japan
[b] Department of Physics and Astronomy, Uppsala University, P.O. Box 516, 75120 Uppsala, Sweden
[c] National Institute for Materials Science (NIMS), 1-2-1 Sengen, Tsukuba 305-0047, Japan
[d] Electron Nanoscopy Section, Advanced Measurement Technology Center, Institute of Materials and Systems for Sustainability, Nagoya University, Furo-cho, Chikusa-ku, Nagoya 464-8603, Japan

ARTICLE INFO

Keywords:
EMCD
FePt network film
Semi-core excitation spectra

ABSTRACT

In this study, we applied electron energy-loss magnetic chiral dichroism (EMCD), an electron counterpart of X-ray magnetic circular dichroism (XMCD), to a network nanostructured FePt $L1_0$ ordered alloy film to examine the relative orientation of magnetic moments between neighboring Fe and Pt atoms using the Fe-$M_{2,3}$, Pt-$O_{2,3}$, and Pt-$N_{6,7}$ semi-core excitation spectra with transmission electron microscopy and electron energy-loss spectroscopy. EMCD signals were successfully extracted from a large number of spectra using a dedicated data analysis procedure to obtain sufficient noise statistics. Results showed that the relative sign relation of the EMCD signals between the Fe and Pt absorption edges was consistent with that of the theoretical dielectric tensor while assuming that parallel magnetic moments exist between neighboring Fe and Pt. We believe the results of this study can be applied to alloys with different nanostructures to determine whether the spin configuration depends on the size and geometry of the nanostructures.

1. Introduction

For years, magnetism has been a key subject in fundamental condensed matter physics and current R&D for engineering applications, such as stronger hard/soft magnets, spintronics, and multiferroics for faster and energy-saving devices. Therefore, it is crucial to establish engineering applications with the macroscopic magnetic properties by controlling the material structures, textures on a nanometric scale, and types and combinations of doped magnetic/non-magnetic elements, which inevitably require access to the local magnetic properties at finer scales. Along with the classical electromagnetic property measurements such as external magnetic fields, magnetization, and their associated properties, modern microscopic measurements that access the origins of magnetism (spin configurations and dynamics, spin/orbital magnetic moments, etc.) directly are currently being made available using spin-polarized electrons (low-energy electron microscopy; SPLEEM [1]), circularly polarized X-rays (X-ray magnetic circular dichroism; XMCD), and neutrons (neutron inelastic scattering; NIES). However, these experimental techniques have their limitations; the LEEM probes the material surfaces only, whereas XMCD and NIES access an area no smaller than a few tens of nanometers.

Electron energy-loss magnetic chiral dichroism (EMCD), an electron counterpart of XMCD, was first proposed theoretically in 2006 (currently referred to as 'classical EMCD'; [2]), and since then has undergone subsequent development both theoretically [3–10] and experimentally. Furthermore, it was branched into several technically varying schemes such as atomic column/plane resolution EMCD, which is an extension of conventional EMCD, and the vortex beam methods utilizing stronger magnetic interactions between the incident probe exhibiting an orbital angular moment and magnetic materials [11–17]. The EMCD

Abbreviations: EMCD, Electron energy-loss magnetic chiral dichroism.

* Corresponding author at: Electron Nanoscopy Section, Advanced Measurement Technology Center, Institute of Materials and Systems for Sustainability, Nagoya University, Furo-cho, Chikusa-ku, Nagoya 464-8603, Japan.
E-mail address: smuto@imass.nagoya-u.ac.jp (S. Muto).

https://doi.org/10.1016/j.jmmm.2022.169522
Received 23 March 2022; Received in revised form 14 May 2022; Accepted 23 May 2022
Available online 25 May 2022

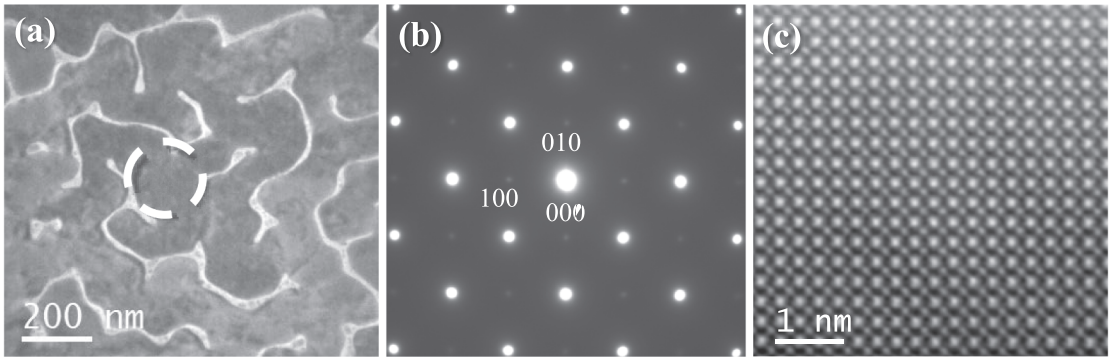

Fig. 1. (a) Bright-field TEM image of Fe-Pt network film. The broken circle inset shows the position where the selected area aperture was inserted for the EMCD measurement, (b) The selected area diffraction pattern in a wide area of the film. The indices of the Bragg reflections inset are referred to with respect to the $L1_0$ tetragonal unit cell, (c) Atomic-column resolution HAADF image of the present Fe-Pt film. The large and small bright dots correspond to the Pt and Fe atomic columns, respectively, which ensures a well ordered superlattice structure of the film.

family of methods supposedly probes sub-nanometric areas, thereby allowing atomic column-by-column measurements; however, they are still recognized as standing at testing stages on model reference materials and cannot be routinely applied to actual material analysis owing to the low signal-to-noise ratio, which makes quantification difficult. Nevertheless, although qualitative, EMCD can be an unrivaled technique for probing fundamental information on the magnetic properties localized in nanometric areas, such as near the grain boundaries, precipitates, and at atomic resolution, such as the relative spin configuration and/or magnitude of magnetic moments between neighboring atoms/planes.

Overall, very little is known about the effects of composition, disorder, and the size and shape of nanostructures on the microscopic magnetic properties of magnetic data storage materials, such as FePt alloys. FePt is essentially used in high-density magnetic data storage applications [18–21] considering it possesses important preconditions such as high saturation magnetization, large magneto-crystalline anisotropy energy, and a high Curie temperature. Therefore, a detailed evaluation of the microscopic magnetic properties is of high importance.

The magnetism of FePt is dominated by large Fe magnetic moments of approximately $3\mu_B$, parallel to the [0 0 1] direction, whereas the Pt magnetic moments are almost an order of magnitude lower [22–24]. Density functional theory (DFT) calculations have reported competition between the ferromagnetic (FM) and antiferromagnetic (AFM) exchange interactions between Fe atoms in FePt, which stabilizes the FM structure with an increase in the substitutional disorder and decrease in tetragonality, that is, when the c/a ratio approaches 1 [25–28]. Moreover, it is argued that the magnetism of Pt atoms is purely induced and hence, contributes to the FM order [29–32]. This is in good agreement with the several experimental evidence, notably by neutron diffraction, X-ray magnetic circular dichroism (XMCD) measurements [33,34], and ground state DFT calculations [24,27].

The relative orientations of Fe and Pt magnetic moments have also been discussed. While XMCD measurements clearly favor parallel (FM) alignment [34], studies have reported neutron diffraction on $Fe_{72}Pt_{28}$ [35] and FePt [36] suggest antiparallel (ferrimagnetic, FIM) ordering of the Fe and Pt magnetic moments to predict the magnetic properties of FePt nanoparticles as a function of their size [19]. In contrast, another neutron diffraction study [33] reported a better fit of the experimental data when a parallel orientation of the Fe and Pt moments was assumed. First-principles calculations of FePt within an FM phase reported a parallel orientation of the Fe and Pt magnetic moments [23–25,30,33], which was in agreement with the XMCD results [34] and the latter neutron diffraction study [33]. The influence of size effects on the magnetism of nanostructured FePt alloys has also been studied [18,19,26], and demonstrated important consequences for their applicability in high-density magnetic recording.

In this study, we combine experimental and theoretical studies on thin FePt films to measure the electron magnetic circular dichroism (EMCD) spectra in the low-loss region, where the Fe-$M_{2,3}$, Pt-$O_{2,3}$, and Pt-$N_{6,7}$ edges are located in the energy-loss range of 50–90 eV. This is a major advantage of EMCD considering multiple absorption edges can be measured in one experiment, unlike XMCD, where multiple beamlines covering different energy regions are required. Another advantage is that the spectral intensities of the low-loss region are significantly higher by one or two orders of magnitude compared to those of the core-loss spectra located at energy losses higher than 200 eV, which shortens the spectral acquisition time and suppresses the electron beam damage of the sample simultaneously. However, EMCD spectra in the low-loss region behave in a complicated manner depending on the momentum transfer vectors operated at two different chiralities, considering the plasmon peak exhibits dispersion depending on the momentum transfer [37] and the diffraction condition set is not strictly symmetric with respect to the conceived mirror axis, which makes the analysis process, such as edge isolation by background subtraction and EMCD signal extraction by difference operation between the isolated spectra having different chirality, difficult. We present the results of the DFT calculations of the electronic structure, spectral properties, and dynamical diffraction effects, which influence the EMCD spectra.

2. Materials and methods

2.1. Fabrication of the FePt network film

A 40 nm thick FePt film was grown epitaxially onto a single-crystal MgO (0 0 1) substrate via DC magnetron co-sputtering using Fe and Pt sources at 600 °C. After deposition of the FePt film, a 25 nm thick C layer was capped to avoid surface contamination. Considering the film is much thicker than the critical thickness for a well-separated microstructure, it exhibits a network-like microstructure. FePt and MgO have an orientational relationship with the cube-on-cube structure. The degree of order estimated from the integrated intensities of the (0 0 1) and (0 0 2) peaks in the XRD pattern is 0.98. To prepare the TEM specimen, the MgO substrate was chemically removed: after thinning the sample about 50 μm by manual grinding, chemical etching of MgO was performed using a solution of phosphoric acid and sulfuric acid mixed at a ratio of 98:2. A temperature of the solution was about 100 °C. Finally the floating remained FePt film was picked up with Cu mesh (200 mesh) and fully dried before TEM observation. TEM inspection showed that the film exhibited a network texture with a typical width of ~200 nm and [0 0 1] normal to the film surface, as shown in Fig. 1(a) and (b), respectively. The thickness of the films was 40 nm ± 5 nm within the area of Fig. 1(a), as estimated by a standard method using low energy-loss spectra. Fig. 1(c) shows an atomic-column resolution high-angular

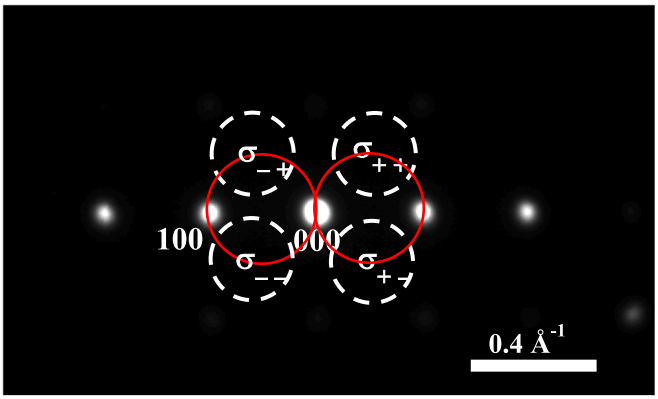

Fig. 2. (a) Diffraction condition for the present EMCD measurement geometry. The circles inset indicate the four quadrants, showing the positions and size of the detector entrance aperture for spectral acquisition. The red circles represent the Thales circles to guide the eyes.

annular dark-field STEM image, which demonstrates good crystallinity and a high-order parameter of the films. Fig. A.1 in Appendix A shows the magnetization hysteresis curve of the present sample.

2.2. EMCD measurement

Spectral data was collected using a Jeol JEM-2100 S/TEM operated at 200 kV, equipped with an EEL spectrometer (Gatan Enfina 1000). Classical EMCD scheme was applied at room temperature, and the film was tilted by approximately 10° from the (0 0 1) zone axis to ensure the diffraction pattern was set as the symmetric 100 systematic row of reflections, as shown in Fig. 2, where the selected area aperture was placed as a broken circle (corresponding to the area of measurement) and the convergent semi angle of the defocused incident electron beam was 1 mrad, as shown in Fig. 1(a). The EEL spectra of low-loss (0–120 eV for Pt-$O_{2,3}$, Fe-$M_{2,3}$, and Pt-$N_{6,7}$ edges) and high-loss (650–780 eV for Fe-$L_{2,3}$ edges) regions were recorded with the detector entrance aperture symmetrically placed at all four quadrants according to the geometry of classical EMCD [2], as shown in Figs. 3 and 4, respectively. Considering an external magnetic field of 1–2 T was applied between the objective pole-piece gap and the microscope optic axis, the chirality of the magnetic signal was determined by the vector product of the two momentum transfer vectors subtended from the Bragg reflections to the detector [2]. The four detector positions were marked as σ_{aa} ($a = +$ or $-$), which corresponded to the four orthants with the x-axis along the 100 systematic row of reflections and the origin at 000. The sign (chirality) of the magnetic signals was supposed to be the same for the diagonal detector positions and the opposite for the same row or column, according to theoretical considerations. For each spectral acquisition, up to 3000 frames were summed up with the energy drift corrected on line using a house-made script program [38], without losing energy resolution, to average the corrected noise of the CCD detector, where the detector energy dispersion was 0.1 eV/channel and the single exposure time for each spectral acquisition was 0.05 s and 1 s for low-loss and high-loss acquisition, respectively. Although the edge onsets are not obvious except for Pt-O_2 and Pt-O_3, they can be easily specified with reference to the unambiguous spectral features of Fe-$M_{2,3}$ and Pt-$N_{6,7}$.

2.3. EMCD signal extraction

The EMCD signal of the Fe-$L_{2,3}$ white line from the high-loss data was extracted as a double difference according to the following formula: EMCD = [σ_{++} - σ_{+-}] - [σ_{-+} - σ_{--}]. This method did not work for the low-loss spectra considering the pre- and post-edge background subtly varied with a slight deviation from the symmetric diffraction condition during the data recording. Therefore, we applied multiple curve resolution

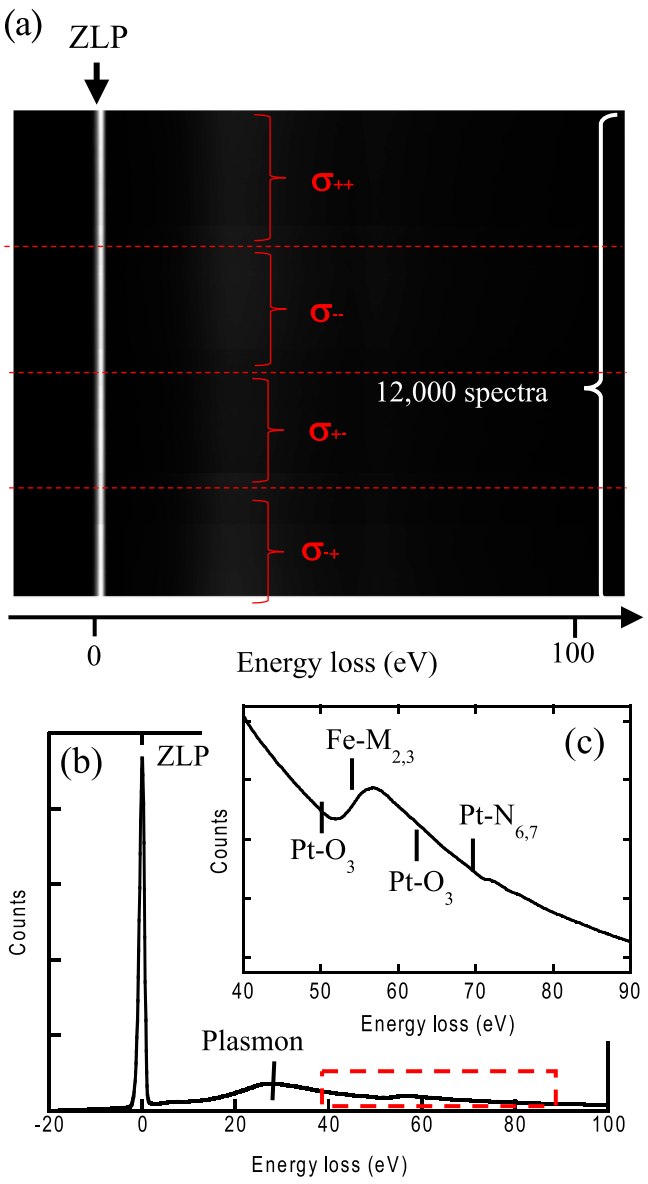

Fig. 3. (a) 2D image data of all 12,000 low-loss spectra recorded with the energy drift corrected on-line: each row corresponds to a single EEL spectrum and 3,000 rows were taken from each quadrant in Fig. 2 of the main text. ZLP: zero-loss peak, (b) Extracted EEL spectrum from (a), and (c) Enlarged image of the red framed area in (b), corresponding to the region of interest in the low-loss region in this study. The position of each absorption edge onset is indicated inset.

(MCR) with appropriate constraints separately to the energy region of 48–62 eV and 58–92 eV, thereby removing the first average spectral feature. Then, we extracted the signal components that change their sign between [σ_{++}, σ_{--}] and [σ_{+-}, σ_{-+}] pairs. Finally, we applied the double difference to the extracted datasets, as described in detail in Appendix B.

2.4. DFT calculation of dielectric tensor

DFT calculations were performed using the full-potential linearized augmented plane wave (FP-(L)APW) method, as implemented in the WIEN2k [39,40] package. We used the generalized gradient approximation (GGA [41]) for the exchange–correlation functional. Atomic sphere radii were set to 2.45 a.u. and 2.50 a.u. for Fe and Pt, respectively (1 a.u. = 0.529178 Angstrom). Approximately 80 basis functions per atom were used to construct a scalar-relativistic eigenvalue problem

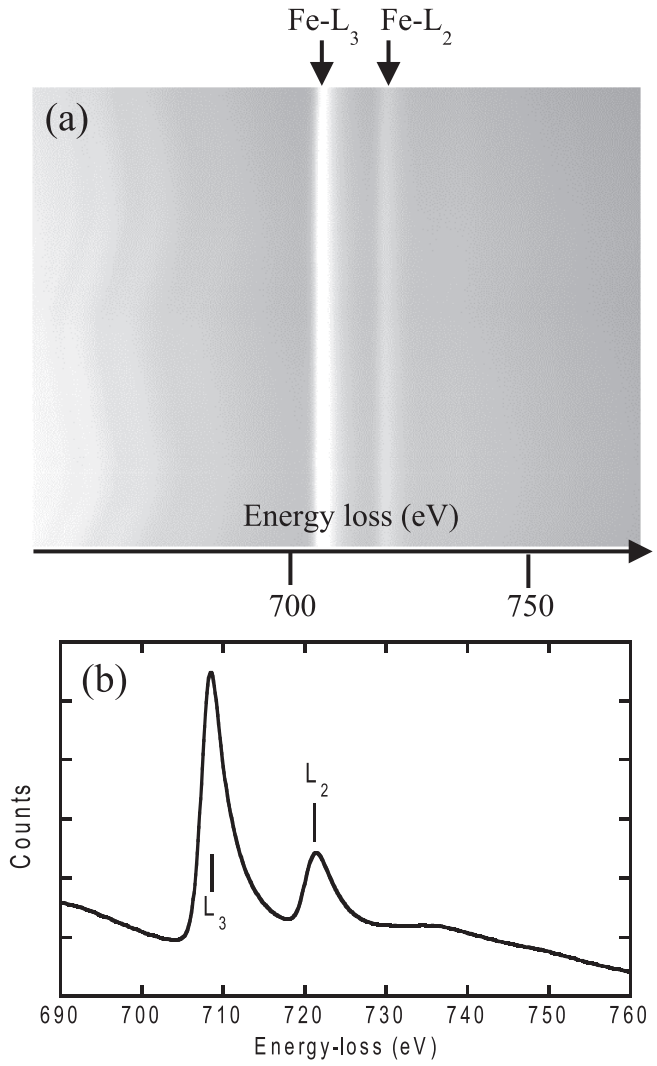

Fig. 4. (a) 2D image data of all 12,000 high-loss spectra recorded with the energy drift corrected on-line, as in Fig. 3(a). The energy drift corrections are visible in the pre-edge background region (left-most side) as the wavy afterglow pattern in the CCD detector and (b) Extracted spectrum from (a). Peak positions are marked for L_2 and L_3 inset.

($RK_{max} = 8.0$). Spin-orbital coupling was included in the second variational step with a base size of approximately 130 scalar-relativistic eigenstates, assuming that the magnetization direction was parallel to the c-axis. The Brillouin zone (BZ) was sampled at 10,000 k-points (702 k-points in the irreducible wedge of the BZ), and BZ integration was performed using the modified tetrahedron method. Spectroscopic calculations for lower-energy edges were performed using the OPTIC package in WIEN2k [42] and their own codes [2,7] for higher-energy edges.

Dynamical diffraction effects for the EELS and EMCD spectra were simulated using MATS.v2 software [8]. The convergence parameter was set to 5×10^{-5}, and both incoming and outgoing electron waves were represented by the Bloch wave method. Approximately 430 plane waves were used to represent Bloch waves inside the crystal. Simulations were performed for sample thicknesses of 40 nm and accelerating voltage of 200 kV, assuming the orientation was in a symmetric systematic row condition (three-beam orientation) with $\mathbf{g} = (100)$ and an approximately 10° tilt from the (001) zone axis orientation.

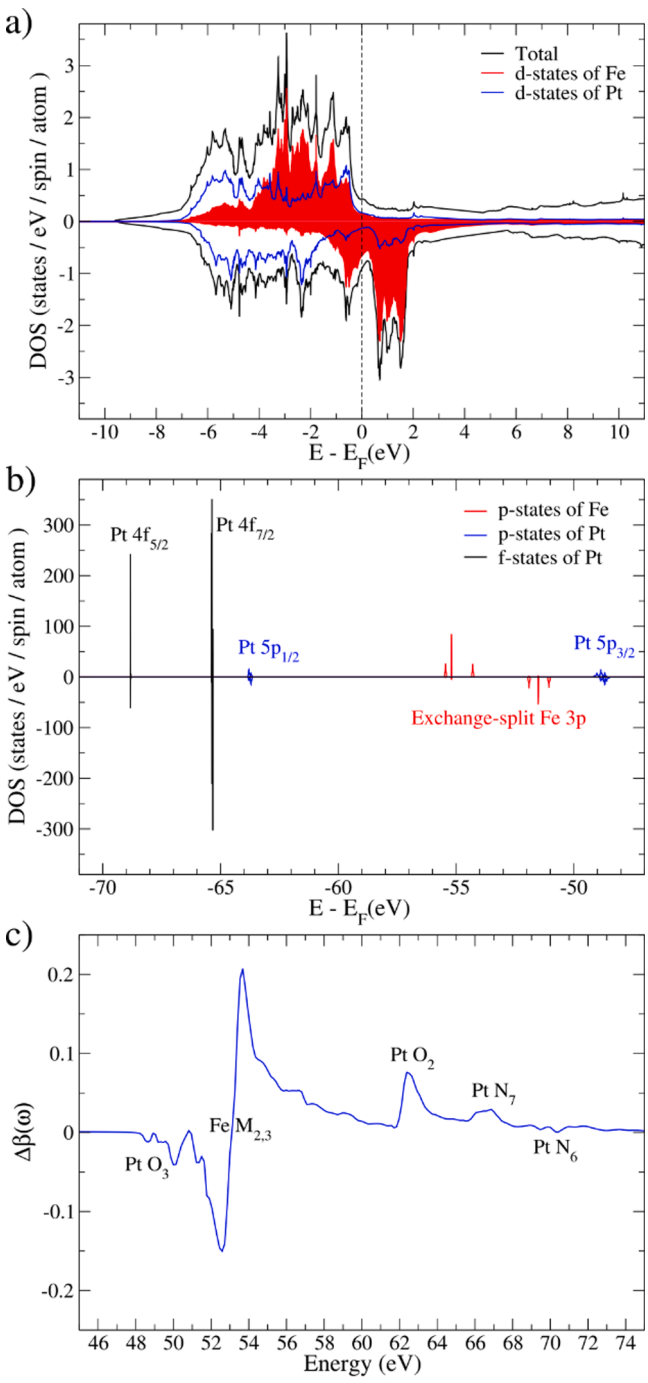

Fig. 5. (a) Spin-resolved density of electronic states within the range of +/- 11 eV around the Fermi level, including projected densities of iron and platinum d-states, respectively, (b) Spin-resolved density of states of semi-core levels within the energy range of −71 eV to −47 eV with respect to the Fermi level (assumed at zero energy), and (c) Magneto-optical function Δβ obtained from calculated matrix elements of the dielectric tensor. Individual features are assigned to core-level edges, following the energy positions of semi-core levels in panel (b).

3. Results and discussion

3.1. Theoretical dielectric tensor to compare with the sign of the magnetic signal

Fig. 5 shows the results of the electronic structure calculations. Fig. 5a shows the spin-resolved electronic densities of states, and the total spin-resolved DOS shows exchange splitting owing to

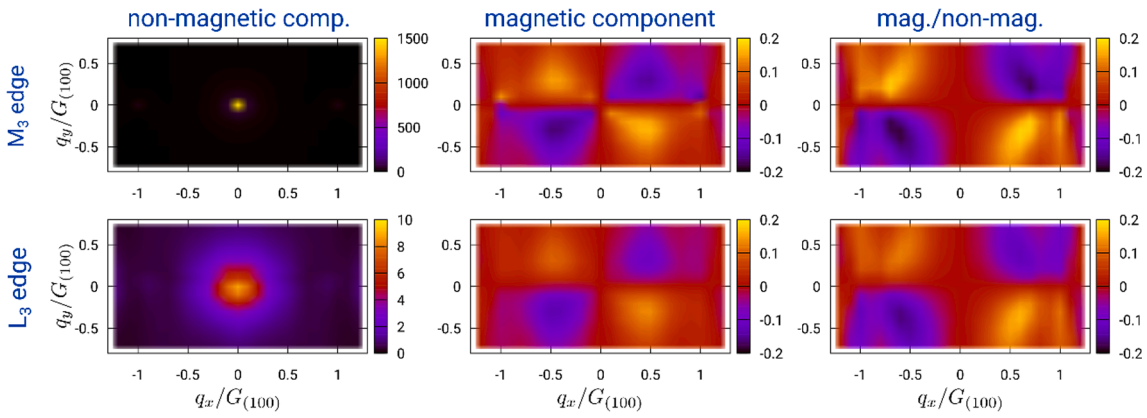

Fig. 6. Simulated signal distributions of non-magnetic, EMCD, and relative EMCD with respect to the non-magnetic signal intensity in the diffraction planes for the sample thickness of 40 nm for Fe-L_3 (top) and -M_3 (bottom) spectra, respectively. The transmitted beam **O** and 100 reflection G are located at (0, 0) and (1, 0), respectively.

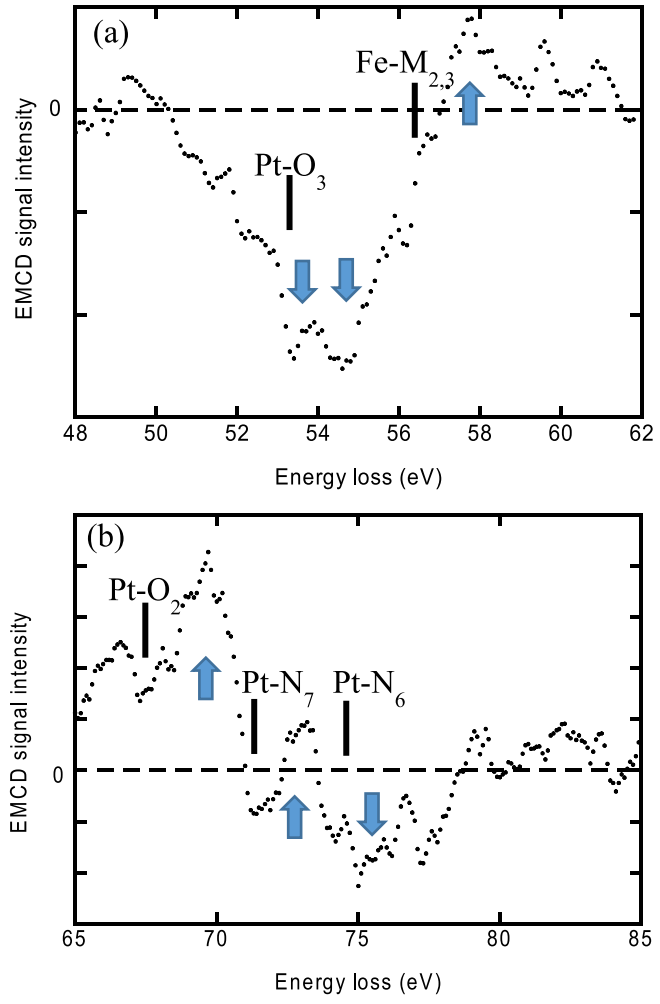

Fig. 7. Final EMCD signals (dots) extracted for Pt-O_3 and Fe-$M_{2,3}$ edges (a), Pt-O_2 and Pt-$N_{6,7}$ edges (b), and the cumulative sum are shown by the solid lines to better visualize each peak feature inset in (a) and (b), with each edge position indicated.

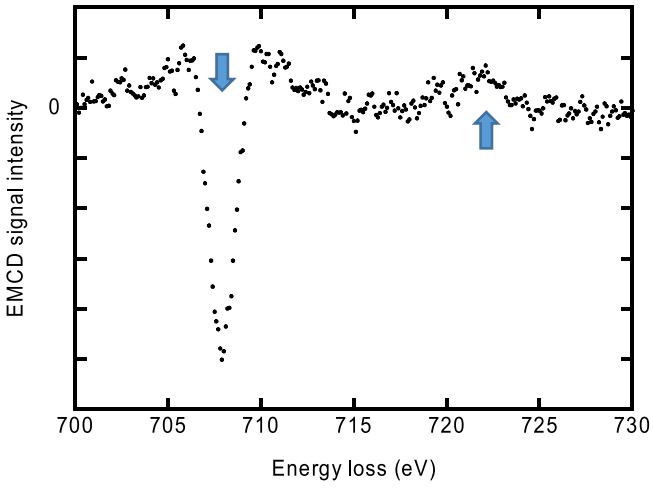

Fig. 8. Final EMCD signal (dots) extracted for Fe-$L_{2,3}$ edge.

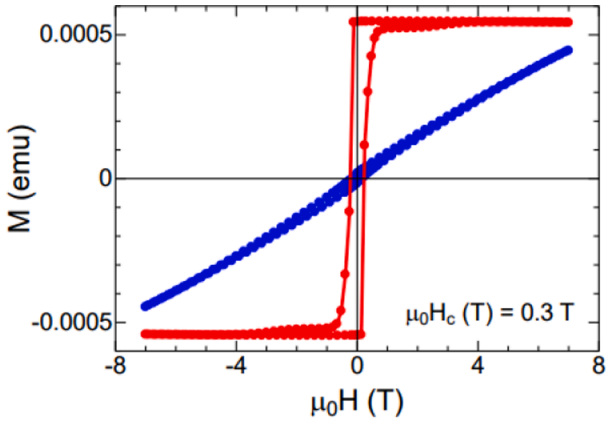

Fig. A.1. Magnetization hysteresis curve of the sample with the external field applied in the directions normal to the film surface (parallel to the c-axis) (red dots and line) and parallel to the film surface (perpendicular to the c-axis) (blue dots and line).

ferromagnetism in the system. Furthermore, the projected DOS of iron d-states shows that the exchange splitting is almost entirely due to iron, whereas it was less pronounced for platinum d-states. However, a clear hybridization was observed with the iron d-states. This is in agreement with published literature [22–24].

Fig. 5b shows the DOS of the semi-core states ranging from −71 eV to −47 eV, which is the energy range of interest in the context of our spectroscopic measurements (see below). In this range, platinum 5p

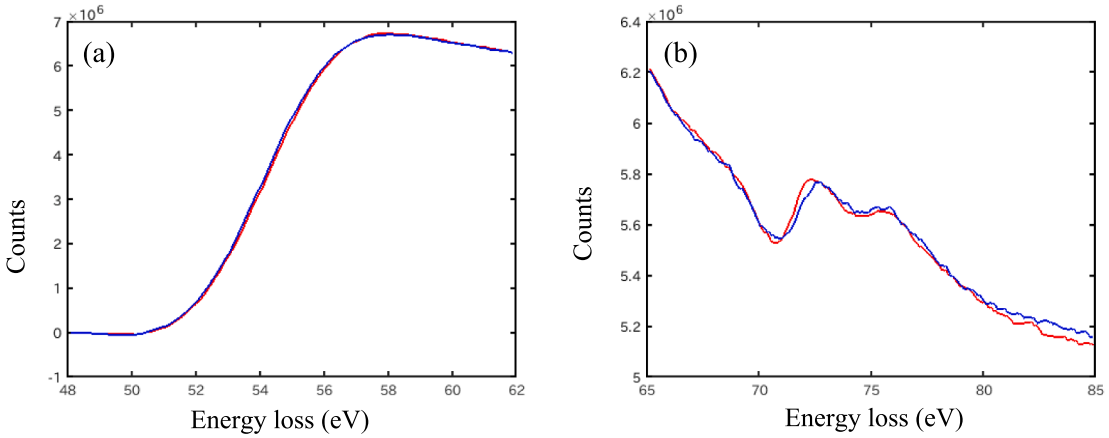

Fig. B.2. Extracted and normalized $D_{\pm}(E)$ spectra (red and blue solid lines, respectively) for the energy regions of 45 eV < E < 65 eV (a) and 65 eV < E < 85 eV (b), respectively.

states split by approximately 16 eV owing to spin–orbit coupling (SOC), and platinum 4f states SOC-split by approximately 4 eV. However, for iron 3p semi-core states, the spin–orbit splitting and exchange are of comparable strength and, hence, it is not possible to clearly assign the $3p_{1/2}$ and $3p_{3/2}$ characters to individual peaks. Iron 3p states are split into six individual peaks with spin-up states having a center of mass energy approximately 3.5 eV lower than the spin-down states. However, this is convenient for circular dichroism experiments owing to the imbalance between the spin-up and spin-down DOS for unoccupied states and the energy shift between the two groups of exchange and SOC-split iron 3p states.

Finally, Fig. 5c shows the magneto-optical function Δβ, which was obtained from the calculated elements of the dielectric tensor (Eq. (4) in Dewhurst [43]: The magneto-optical function Δβ can be directly compared to the magnetic circular dichroism measured in experiments; therefore, the relative signs of individual peaks in Fig. 5c represent the DFT prediction of experiments for the parallel spin orientation of Fe and Pt magnetic moments. It should be noted that the onset energies of the absorption edges are underestimated by a few eVs in the present DFT calculations, compared with the experimental values.

Simulated EMCD signal distributions in the diffraction plane are shown in Fig. 6, primarily to check if the relative sign reversal of the EMCD signals takes place. Simulations show a very similar pattern of magnetic signal distribution for both edges. The main difference can be observed for the non-magnetic signal, showing an expected increased broadening of Bragg peaks at higher energy loss.

3.2. *Extracted EMCD signals and spin configuration derived*

Fig. 7(a) and (b) show the final EMCD signals extracted for the Pt-O_3 and Fe-$M_{2,3}$ edges and the Pt-O_2 and Pt-$N_{6,7}$ edges, respectively. It should be noted that the background is a constant slowly decaying slope underlying the EMCD signals in (b), presumably due to plasmon dispersion [37], which makes the sign of the signals ambiguous with respect to the reference horizontal broken line. However, the sign of the signals would be obvious judging from the convex/concave nature of the neighboring signals, as indicated by the up/down arrows inset in the figure.

Fig. 8 shows the EMCD signal extracted from the Fe-$L_{2,3}$ edge. The sign relationship in Fe-$M_{2,3}$ exhibits a minus/plus relation, which is consistent with that between Fe-L_3 and Fe-L_2 in the magnetization direction. This relationship ensures consistency of the measurements acquired for Fe in [44] with the dynamical scattering effects taken into account, as shown in Fig. 6. Therefore, we can conclude that the relative sign between Pt-O_2 and Pt-N_7 is the same, which is consistent with the theoretical calculation results shown in Fig. 5(c). Additionally, the relative sign between Pt-O_2 and Fe-$M_{2,3}$ also exhibits a relationship that corresponds to that in Fig. 5(c), which indicates that the relative spin relationship between Fe and Pt should be parallel.

4. Conclusion

In this study, we extracted the EMCD signal of a nanostructured binary alloy using multiple core-loss spectra, including semi-core excitations in TEM-EELS, which can be detected in parallel in a single experiment. We fabricated an $L1_0$-type ordered FePt alloy film with a network structure to measure Pt-$O_{2,3}$, Fe-$M_{2,3}$, and Pt-$N_{6,7}$ located in the energy region range of 40–80 eV. EMCD signals were successfully extracted by applying the classical EMCD method with dedicated data processes. Results showed that the relative signs of the extracted magnetic signals were comparable with the theoretical dielectric tensor, thereby indicating that the relative orientation of the magnetic moment between neighboring Fe and Pt atoms should be parallel, as expected. Furthermore, the extracted magnetic moment direction was found to be consistent with the EMCD from the Fe-$L_{2,3}$ edge measured separately.

The results of this study can be widely applied to nanostructures of magnetic materials with a nanometric resolution to qualitatively determine the relative orientation of neighboring atoms with a small-scale laboratory instrument. We are currently investigating different types of nanostructured FePt films, such as nanoparticles, to examine whether the relative spin direction depends on the nanostructure.

CRediT authorship contribution statement

Hitoshi Makino: Investigation, Writing – original draft. **Ján Rusz:** Conceptualization, Formal analysis, Writing – original draft, Writing – review & editing. **Jian Wang:** Resources. **Diego Turenne:** Resources. **Masahiro Ohtsuka:** Methodology. **Yukiko K. Takahashi:** Resources, Writing – original draft. **Hermann A. Dürr:** Conceptualization, Project administration. **Shunsuke Muto:** Investigation, Project administration, Writing – original draft, Writing – review & editing, Supervision, Funding acquisition.

Declaration of Competing Interest

The authors declare that they have no known competing financial interests or personal relationships that could have appeared to influence the work reported in this paper.

Acknowledgments

We would like to thank Editage (www.editage.com) for English

language editing. This work was supported in part by a Grant-in-Aid for Scientific Research (KAKENHI) (A) (Grant Number 21H04616) from the Japan Society for the Promotion of Science. J.R. acknowledges financial support of Swedish Research Council and Carl Tryggers foundation. The simulations were enabled by resources provided by the Swedish National Infrastructure for Computing (SNIC), partially funded by the Swedish Research Council through grant agreement no. 2018-05973.

Appendix A. . Magnetization hysteresis curve of the present sample

See Fig. A.1.

Appendix B. . Detailed EMCD signal extraction procedure for low-loss region

Considering the volume plasmon peak is sensitive to the sample thickness in its intensity and exhibits a dispersion dependent on the momentum transfer associated with the energy loss, the nonmagnetic signal background changes not only with the sample thickness but also with a slight deviation in the detector position from the symmetric one, which influences the simple mutual subtraction procedure between the two spectra with opposite chirality to extract the magnetic signals.

Given that it is not easy to correctly predict the variable background slope owing to the plasmon dispersion, we assumed that the raw spectrum, D_{raw}, can be expressed by a linear combination of the non-magnetic background, S_{NM}, and the magnetic signal, S_{EMCD}, as a function of energy loss, E, with the known sign of the weight, W_{EMCD}, for the S_{EMCD} depending on the chirality:

$$D_{raw}(E) = S_{NM}(E) + s_{chirality}\Omega_{EMCD}S_{EMCD}(E) \tag{B1}$$

where S_{NM} is the averaged spectrum over the entire spectra and

$$s_{chirality}\Omega_{EMCD} < 0 \; and \; > 0 \; for \; chirality + and - \; respectively \tag{B2}$$

For experimental data, Eq. (B.1) can be expressed in matrix form as:

$$D_{raw} = WS \tag{B3}$$

where the matrix **W** includes the factor $s_{\mathrm{chirality}}$ for the unified description, and

$$D_{raw} = \left\{D_{raw}^{i,j}\right\}, i = 1, \cdots, N_C; j = 1, \cdots, N_E \tag{B4}$$

N_{C} is the total number of spectra and N_E is the number of energy channels of the detector

$$W = \{Wi,j\} = (1, \; schirality \; i,j \;), i = 1, \ldots, N_C; \; j = 1, \ldots, NE, \tag{B5}$$

where according to Fig. 3(a),

$$s_{chirality} = \begin{cases} 1 & for + chirality : i = 1 - 6,000 \\ -1 & for - chirality : i = 6,001 - 12,000 \end{cases} \tag{B6}$$

$$\mathbf{S} = \left\{S_{i,j}\right\} = \begin{pmatrix} S_{NM} \\ S_{EMCD}^{j} \end{pmatrix}, j = 1, \cdots, N_E. \tag{B7}$$

Then, the extracted components are averaged over the same chirality, and finally we obtain:

$$D_{\pm}(E) = S_{NM}(E) + \frac{\left(\sum_i s_{chirality}\Omega_i(E)S_{EMCD}(E)\right)}{\frac{N_C}{2}}, \tag{B8}$$

where $for + chirality : i = 1 - 6,000$ and $for - chirality : i = 6,001 - 12,000$

Eq. (B.3) can be solved starting with an initial value of $\Omega_{i,j} \sim 0.1$, using the fixed S_{NM}^{j} and the constraint in Eq. (B.6) imposed in every iteration loop with the modified alternating least-square (MALS) algorithm [45,46]. The extracted $D_{\pm}(E)$ are noise-averaged spectra, which were normalized by the averaged post-edge intensities ranging between 58 and 62 eV and 78–84 eV for the lower energy region, including the Pt-O_3 and Fe-$M_{2,3}$ edges, and the higher energy region, including the Pt-O_2 and Pt-$N_{6,7}$ edges, respectively.

Since the first primary component is fixed at the largest non-magnetic component, $S_{\mathrm{NM}}(E)$, the other component should include the magnetic component, $S_{\mathrm{EMCD}\pm}(E)$, and q_y-dependent background owing to the plasmon dispersion. In principle, the latter is inseparable from the former considering it varies from one spectrum to another. The extracted spectra ($D_{\pm}(E)$) were separated into two parts: 45 eV $< E <$ 65 eV and 65 eV $< E <$ 85 eV, each normalized by the average intensity for the first 5 eV region. The extracted and normalized $D_{\pm}(E)$ spectra are shown in Fig. B.2 (a) and (b) for the energy regions of 45 eV $< E <$ 65 eV and 65 eV $< E <$ 85 eV, respectively. The slopes of the pre- and post-edge backgrounds in Fig. B.2(b) exhibited obvious discrepancies owing to the q_y-dependent plasmon dispersion, which gives rise to an energy-dependent offset in the final difference spectrum. This could be an origin of the non-zero values of both ends of the final data.

The final results were obtained by subtracting $D_{+}(E)$ from $D_{-}(E)$, as shown in Fig. 6(a) and (b) in the main manuscript.

References

[1] Y. Zhu (Ed.), Spin-polarized low-energy electron microscopy (SPLEEM), in: Modern Techniques for Characterizing Magnetic Materials, Springer, Boston, Massachusetts, 2005, pp. 361–379. 10.1007/0-387-23395-4_9.

[2] P. Schattschneider, S. Rubino, C. Hébert, J. Rusz, J. Kuneš, P. Novák, E. Carlino, M. Fabrizioli, G. Panaccione, G. Rossi, Detection of magnetic circular dichroism using a transmission electron microscope, Nature 441 (2006) 486–488, https://doi.org/10.1038/nature04778.

[3] J. Rusz, S. Rubino, P. Schattschneider, First-principles theory of chiral dichroism in electron microscopy applied to 3 d ferromagnets, Phys. Rev. B. 75 (2007), https://doi.org/10.1103/PhysRevB.75.214425, http://www.ncbi.nlm.nih.gov/pubmed/214425.

[4] J. Rusz, O. Eriksson, P. Novák, P.M. Oppeneer, Sum rules for electron energy loss near edge spectra, Phys. Rev. B. 76 (2007), https://doi.org/10.1103/PhysRevB.76.060408.

[5] L. Calmels, F. Houdellier, B. Warot-Fonrose, C. Gatel, M.J. Hÿtch, V. Serin, E. Snoeck, P. Schattschneider, Experimental application of sum rules for electron energy loss magnetic chiral dichroism, Phys. Rev. B. 76 (2007), https://doi.org/10.1103/PhysRevB.76.060409.

[6] S. Löffler, P. Schattschneider, A software package for the simulation of energy-loss magnetic chiral dichroism, Ultramicroscopy. 110 (2010) 831–835, https://doi.org/10.1016/j.ultramic.2010.02.044.

[7] J. Rusz, S. Rubino, O. Eriksson, P.M. Oppeneer, K. Leifer, Local electronic structure information contained in energy-filtered diffraction patterns, Phys. Rev. B. 84 (2011), https://doi.org/10.1103/PhysRevB.84.064444.

[8] J. Rusz, Modified automatic term selection v2: a faster algorithm to calculate inelastic scattering cross-sections, Ultramicroscopy. 177 (2017) 20–25, https://doi.org/10.1016/j.ultramic.2017.01.008.

[9] S. Löffler, W. Hetaba, Convergent-beam EMCD: benefits, pitfalls and applications, Microscopy (Oxf). 67 (2018) i60–i71, https://doi.org/10.1093/jmicro/dfx129.

[10] J. Barthel, J. Mayer, J. Rusz, P.-L. Ho, X.Y. Zhong, M. Lentzen, R.E. Dunin-Borkowski, K.W. Urban, H.G. Brown, S.D. Findlay, L.J. Allen, Understanding electron magnetic circular dichroism in a transition potential approach, Phys. Rev. B. 97 (14) (2018), https://doi.org/10.1103/PhysRevB.97.144103.

[11] J.C. Idrobo, J. Rusz, J. Spiegelberg, M.A. McGuire, C.T. Symons, R.R. Vatsavai, C. Cantoni, A.R. Lupini, Detecting magnetic ordering with atomic size electron probes, Adv. Struct. Chem. Imag. 2 (2016) 1–10, https://doi.org/10.1186/s40679-016-0019-9.

[12] J. Rusz, S. Muto, J. Spiegelberg, R. Adam, K. Tatsumi, D.E. Bürgler, P.M. Oppeneer, C.M. Schneider, Magnetic measurements with atomic-plane resolution, Nat. Commun. 7 (2016) 12672, https://doi.org/10.1038/ncomms12672.

[13] T. Thersleff, J. Rusz, B. Hjörvarsson, K. Leifer, Detection of magnetic circular dichroism with subnanometer convergent electron beams, Phys. Rev. B. 94 (2016), https://doi.org/10.1103/PhysRevB.94.134430, http://www.ncbi.nlm.nih.gov/pubmed/134430.

[14] J. Verbeeck, H. Tian, P. Schattschneider, Production and application of electron vortex beams, Nature. 467 (2010) 301–304, https://doi.org/10.1038/nature09366.

[15] J. Rusz, S. Bhowmick, M. Eriksson, N. Karlsson, Scattering of electron vortex beams on a magnetic crystal: towards atomic-resolution magnetic measurements, Phys. Rev. B. 89 (2014), https://doi.org/10.1103/PhysRevB.89.134428.

[16] D. Song, A.H. Tavabi, Z.A. Li, A. Kovács, J. Rusz, W. Huang, G. Richter, R.E. Dunin-Borkowski, J. Zhu, An in-plane magnetic chiral dichroism approach for measurement of intrinsic magnetic signals using transmitted electrons, Nat. Commun. 8 (2017) 15348, https://doi.org/10.1038/ncomms15348.

[17] Z. Wang, A.H. Tavabi, L. Jin, J. Rusz, D. Tyutyunnikov, H. Jiang, Y. Moritomo, J. Mayer, R.E. Dunin-Borkowski, R. Yu, J. Zhu, X. Zhong, Atomic scale imaging of magnetic circular dichroism by achromatic electron microscopy, Nat. Mater. 17 (2018) 221–225, https://doi.org/10.1038/s41563-017-0010-4.

[18] S. Sun, Recent advances in chemical synthesis, self-assembly, and applications of FePt nanoparticles, Adv. Mater. 18 (2006) 393–403, https://doi.org/10.1002/adma.200501464.

[19] T. Huang, H. Wang, Y. Zou, W. Cheng, C. Xie, Explorations on size limit of $L1_0$-FePt nanoparticles for practical magnetic storage, AIP Adv. 6 (2016), https://doi.org/10.1063/1.4967243, http://www.ncbi.nlm.nih.gov/pubmed/115302.

[20] A.Q. Wu, E.K.C. Chang, Y. Zhao, H. Zhou, K. Gao, J. Thiele, M. Seigler, G. Ju, E. Gage, Y. Kubota, T. Klemmer, T. Rausch, C. Peng, Y. Peng, D. Karns, X. Zhu, Y. Ding, HAMR areal density demonstration of 1+ Tbpsi on Spinstand, IEEE Trans. Magn. 49 (2013) 779–782, https://doi.org/10.1109/TMAG.2012.2219513.

[21] D. Weller, G. Parker, O. Mosendz, E. Champion, B. Stipe, X. Wang, T. Klemmer, G. Ju, A. Ajan, A.H.A.M.R. Media, Technology road map to an areal density of 4 Tb/in^2, IEEE Trans. Magn. 50 (2014) 1–8, https://doi.org/10.1109/TMAG.2013.2281027.

[22] Z. Lu, R.V. Chepulskii, W.H. Butler, First-principles study of magnetic properties of $L1_0$-ordered MnPt and FePt alloys, Phys. Rev. B. 81 (2010), https://doi.org/10.1103/PhysRevB.81.094437, http://www.ncbi.nlm.nih.gov/pubmed/094437.

[23] T. Burkert, O. Eriksson, S.I. Simak, A.V. Ruban, B. Sanyal, L. Nordström, J.M. Wills, Magnetic anisotropy of $L1_0$ FePt and $Fe_{1-x}Mn_xPt$, Phys. Rev. B. 71 (2005), https://doi.org/10.1103/PhysRevB.71.134411, http://www.ncbi.nlm.nih.gov/pubmed/134411.

[24] J.B. Staunton, S. Ostanin, S.S.A. Razee, B. Gyorffy, L. Szunyogh, B. Ginatempo, E. Bruno, Long-range chemical order effects upon the magnetic anisotropy of FePt alloys from an ab initio electronic structure theory, J. Phys.: Condens. Matter. 16 (2004) S5623–S5631, https://doi.org/10.1088/0953-8984/16/48/019.

[25] G. Brown, B. Kraczek, A. Janotti, T.C. Schulthess, G.M. Stocks, D.D. Johnson, Competition between ferromagnetism and antiferromagnetism in FePt, Phys. Rev. B. 68 (2003), https://doi.org/10.1103/PhysRevB.68.052405, http://www.ncbi.nlm.nih.gov/pubmed/052405.

[26] C. Barreteau, D. Spanjaard, Magnetic and electronic properties of bulk and clusters of FePt $L1_0$, J. Phys. Cond. Matt. 24 (2012) 406004, https://doi.org/10.1088/0953-8984/24/40/406004.

[27] H.-B. Luo, W.-X. Xia, J. Du, J. Zhang, J.P. Liu, A. Yan, On the magnetic structure of $(Fe_{1-x}Mn_x)Pt$: A first-principles study, J. Magn. Magn. Mater. 378 (2015) 138–142 (142). 10.1016/j.jmmm.2014.11.034.

[28] R. Skomski, A. Kashyap, J. Zhou, Atomic and micromagnetic aspects of L10 magnetism, Scr. Mater. 53 (2005) 389–394, https://doi.org/10.1016/j.scriptamat.2005.04.036.

[29] O.N. Mryasov, Magnetic interactions in 3d–5d layered ferromagnets, J. Magn. Magn. Mater. 272–276 (2004) 800–801, https://doi.org/10.1016/j.jmmm.2003.11.285.

[30] O.N. Mryasov, Magnetic interactions and phase transformations in FeM, M = (Pt, Rh) ordered alloys, Phase Trans. 78 (2005) 197–208, https://doi.org/10.1080/01411590412331316591.

[31] X.B. Liu, Z. Altounian, Exchange interaction in $L1_0$-ordered FePt and Copt from first-principles, J. Appl. Phys. 109 (2011) 07B762, https://doi.org/10.1063/1.3564953.

[32] O.N. Mryasov, U. Nowak, K.Y. Guslienko, R.W. Chantrell, Temperature-dependent magnetic properties of FePt: effective spin Hamiltonian model, Europhys. Lett. 69 (2005) 805–811, https://doi.org/10.1209/epl/i2004-10404-2.

[33] J. Lyubina, I. Opahle, M. Richter, O. Gutfleisch, K.-H. Müller, L. Schultz, O. Isnard, Influence of composition and order on the magnetism of Fe–Pt alloys: neutron powder diffraction and theory, Appl. Phys. Lett. 89 (2006), https://doi.org/10.1063/1.2222244, http://www.ncbi.nlm.nih.gov/pubmed/032506.

[34] C. Antoniak, M. Farle, MAGNETISM AT THE nanoscale: the CASE OF FePt, Mod. Phys. Lett. B. 21 (2007) 1111–1131, https://doi.org/10.1142/S0217984907013821.

[35] P.J. Brown, T. Chatterji, J. Kästner, K.R.A. Ziebeck, Magnetization distribution in the ordered Fe 72 Pt 28 Invar alloy, J. Phys.: Condens. Matter. 16 (2004) 5349–5358, https://doi.org/10.1088/0953-8984/16/29/024.

[36] S. Akiyama, Y. Tsunoda, Magnon and magnetic structure of FePt alloy, J. Magn. Magn. Mater. 310 (2007) 1844–1846, https://doi.org/10.1016/j.jmmm.2006.10.625.

[37] M. Rocca, M., U. Valbusa, F. Moresco, on plasmon dispersion measurements by EELS, Surface science, in: F.A. Ponce, M. Cardona (Eds.). Springer, Proceedings in Physics, vol. 62, Springer, Berlin, Heidelberg, 1992. 10.1007/978-3-642-76376-2_8.

[38] Y. Sasano, S. Muto, Energy-drift correction of electron energy-loss spectra from prolonged data accumulation of low SNR signals, J. Electron Microsc. (Tokyo) 57 (2008) 149–158, https://doi.org/10.1093/jmicro/dfn014.

[39] P. Blaha, K. Schwarz, F. Tran, R. Laskowski, G.K.H. Madsen, L.D. Marks, WIEN2k: an APW+lo program for calculating the properties of solids, J. Chem. Phys. 152 (2020) 074101, https://doi.org/10.1063/1.5143061.

[40] P. Blaha, K. Schwarz, G.K.H. Madsen, D. Kvasnicka, J. Luitz, R. Laskowski, F. Tran, L.D. Marks, WIEN2k, an Augmented Plane Wave + Local Orbitals Program for Calculating Crystal Properties (Karlheinz Schwarz, Techn. Universität Wien, Austria). ISBN 3-9501031-1-2, 2018.

[41] J.P. Perdew, K. Burke, M. Ernzerhof, Generalized gradient approximation made simple, Phys. Rev. Lett. 77 (1996) 3865–3868, https://doi.org/10.1103/PhysRevLett.77.3865.

[42] C. Ambrosch-Draxl, J.O. Sofo, Linear optical properties of solids within the full-potential linearized augmented planewave method, Comput. Phys. Commun. 175 (2006) 1–14, https://doi.org/10.1016/j.cpc.2006.03.005.

[43] J.K. Dewhurst, F. Willems, P. Elliott, Q.Z. Li, CvK. Schmising, C, Strüber, D.W. Engel, S. Eisebitt, S. Sharma, Element Specificity of Transient Extreme Ultraviolet Magnetic Dichroism, Phys. Rev. Lett. 124 (2020) 077203. 10.1103/PhysRevLett.124.077203.

[44] Y. Kubota, Y. Hirata, J. Miyawaki, S. Yamamoto, H. Akai, R. Hobara, S. Yamamoto, K. Yamamoto, T. Someya, K. Takubo, Y. Yokoyama, M. Araki, M. Taguchi, Y. Harada, H. Wadati, M. Tsunoda, R. Kinjo, A. Kagamihata, T. Seike, M. Takeuchi, T. Tanaka, S. Shin, I. Matsuda, Determination of the element-specific complex permittivity using a soft x-ray phase modulator, Phys. Rev. B. 96 (2017), https://doi.org/10.1103/PhysRevB.96.214417, http://www.ncbi.nlm.nih.gov/pubmed/214417.

[45] J.-H. Wang, P.K. Hopke, T.M. Hancewicz, S.L. Zhang, Application of modified alternating least squares regression to spectroscopic image analysis, Anal. Chim. Acta. 476 (2003) 93–109, https://doi.org/10.1016/S0003-2670(02)01369-7.

[46] S. Muto, T. Yoshida, K. Tatsumi, Diagnostic nano-analysis of materials properties by multivariate curve resolution applied to spectrum images by S/TEM-EELS, Mater. Trans. 50 (2009) 964–969, https://doi.org/10.2320/matertrans.MC200805.